UCLA
UCLA Previously Published Works

Title

Multiplexed imaging reveals an IFN-γ-driven inflammatory state in nivolumab-associated gastritis

Permalink

https://escholarship.org/uc/item/8j06f73b

Journal

Cell Reports Medicine, 2(10)

ISSN

2666-3791

Authors

Ferrian, Selena
Liu, Candace C
McCaffrey, Erin F
et al.

Publication Date

2021-10-01

DOI

10.1016/j.xcrm.2021.100419

Peer reviewed

eScholarship.org Powered by the California Digital Library
University of California

Cell Reports
Medicine

Report

Multiplexed imaging reveals an IFN-γ-driven inflammatory state in nivolumab-associated gastritis

Graphical abstract

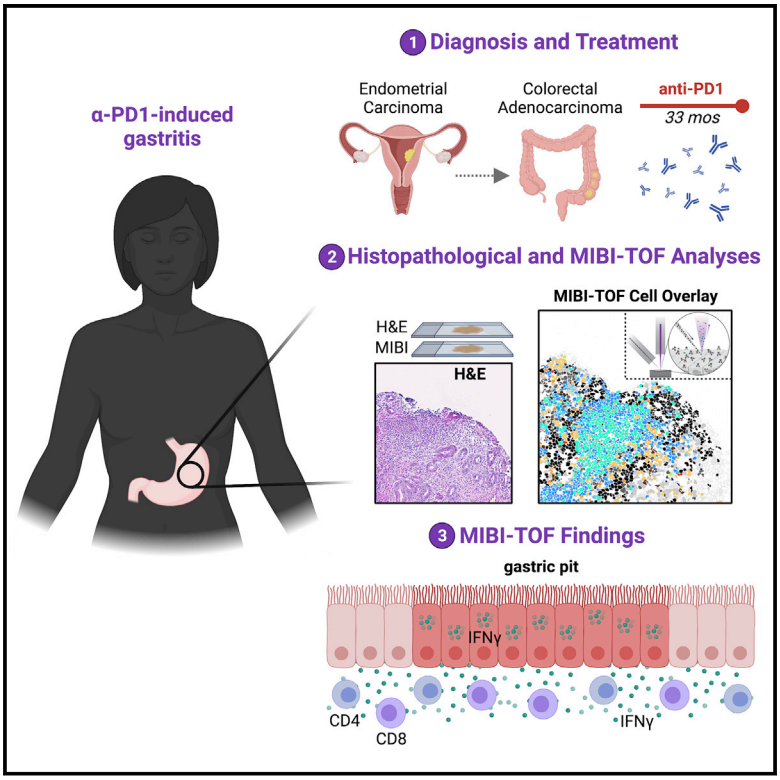

Highlights

- Multiplexed imaging of gastric toxicity associated with anti-PD-1 immunotherapy
- Analysis reveals severe mucosal injury associated with IFN-γ-expressing epithelial cells
- Inflamed gastric epithelium is accompanied by mixed infiltration of CD4 and CD8 T cells

Authors

Selena Ferrian, Candace C. Liu, Erin F. McCaffrey, ..., Antoni Ribas, Sean C. Bendall, Michael Angelo

Correspondence

mangelo0@stanford.edu

In brief

Ferrian et al. leverage multiplexed ion beam imaging by time-of-flight to characterize a case of anti-PD-1-associted autoimmune gastritis. This study reveals gastritis characterized by severe mucosal injury, IFN-γ-producing gastric epithelial cells, and inflammation that includes CD8 and CD4 T cell infiltrates with reduced expression of granzyme B and FOXP3, respectively.

Ferrian et al., 2021, Cell Reports Medicine 2, 100419
October 19, 2021 © 2021 The Author(s).
https://doi.org/10.1016/j.xcrm.2021.100419

CellPress

Cell Reports Medicine

CellPress
OPEN ACCESS

Report

Multiplexed imaging reveals an IFN-γ-driven inflammatory state in nivolumab-associated gastritis

Selena Ferrian,[1] Candace C. Liu,[1] Erin F. McCaffrey,[1] Rashmi Kumar,[1] Theodore S. Nowicki,[2,3,4] David W. Dawson,[4,5] Alex Baranski,[1] John A. Glaspy,[5,6] Antoni Ribas,[3,4,6,7,8,9] Sean C. Bendall,[1,9] and Michael Angelo[1,10,*]

[1]Department of Pathology, Stanford University, Stanford, CA 94305, USA
[2]Department of Pediatrics, Division of Pediatric Hematology/Oncology, University of California, Los Angeles, Los Angeles, CA 90095, USA
[3]Eli and Edythe Broad Center for Regenerative Medicine and Stem Cell Research, University of California, Los Angeles, Los Angeles, CA 90095, USA
[4]Jonsson Comprehensive Cancer Center, David Geffen School of Medicine at UCLA, Los Angeles, CA 90095, USA
[5]Department of Pathology and Laboratory Medicine, David Geffen School of Medicine at the University of California, Los Angeles, Los Angeles, CA 90095, USA
[6]Division of Hematology-Oncology, Department of Medicine, University of California, Los Angeles, Los Angeles, CA 90024, USA
[7]Division of Surgical-Oncology, Department of Surgery, University of California, Los Angeles, Los Angeles, CA 90024, USA
[8]Department of Molecular and Medical Pharmacology, University of California, Los Angeles, Los Angeles, CA 90095, USA
[9]Parker Institute for Cancer Immunotherapy, San Francisco, CA 94129, USA
[10]Lead contact
*Correspondence: mangelo0@stanford.edu
https://doi.org/10.1016/j.xcrm.2021.100419

SUMMARY

Immune checkpoint blockade using PD-1 inhibition is an effective approach for treating a wide variety of cancer subtypes. While lower gastrointestinal (GI) side effects are more common, upper gastrointestinal adverse events are rarely reported. Here, we present a case of nivolumab-associated autoimmune gastritis. To elucidate the immunology underlying this condition, we leverage multiplexed ion beam imaging by time-of-flight (MIBI-TOF) to identify the presence and proportion of infiltrating immune cells from a single section of biopsy specimen. Using MIBI-TOF, we analyze formalin-fixed, paraffin-embedded human gastric tissue with 28 labels simultaneously. Our analyses reveal a gastritis characterized by severe mucosal injury, interferon gamma (IFN-γ)-producing gastric epithelial cells, and mixed inflammation that includes CD8 and CD4 T cell infiltrates with reduced expression of granzyme B and FOXP3, respectively. Here, we provide a comprehensive multiplexed histopathological mapping of gastric tissue, which identifies IFN-γ-producing epithelial cells as possible contributors to the nivolumab-associated gastritis.

INTRODUCTION

The programmed death 1 (PD-1) immune checkpoint is a negative regulator of T cell immune function that prevents cytotoxic T cell activation by self-antigens.[1,2] Inhibition of this target by PD-1 or PD-ligand 1 (PD-L1)-blocking antibodies, such as pembrolizumab or nivolumab, results in increased activation of the immune system and has been used to treat advanced melanoma, non-small cell lung carcinoma, and other malignancies.[1,3,4] Immune-mediated adverse events in the gastrointestinal (GI) tract, including autoimmune enteropathy, autoimmune colitis, and inflammatory bowel disease (IBD)-like colitis, are well-known but infrequent phenomena when these agents are used as a single therapy.[5–9] In particular, colitis is more frequent when used in combination with an anti-CTLA-4 antibody, such as ipilimumab. Most patients with GI tract injury associated with PD-1 blockade treatment present with diarrhea, which occurs in 11%–20% of recipients when used as monotherapy.[10,11] The inflammatory process usually involves multiple sites, while isolated gastritis is rare.[8,9,12,13]

Interferon-γ (IFN-γ) is the signature cytokine generated by $CD4^+$ T helper 1 (Th1) and $CD8^+$ T effector cells, but its exact role in regulating epithelial cell changes is unknown. Several studies have reported the importance of $CD4^+$ regulatory T cells in suppressing cytokines and reducing the severity of gastritis and oxyntic atrophy.[14,15] However, $CD4^+$ T cells that produce IFN-γ (Th1), interleukin-17 (IL-17) (Th17), and IL-4 (Th2) are capable of inducing gastritis and oxyntic atrophy, although to varying degrees and with different types of gastric pathology.[16,17] Epithelial cells are also a source of cytokines that may regulate gastritis, including IFN-γ, IL-1β, IL-6, and IL-33.[18] Finally, neutrophils contribute to the severity of gastritis and mediate epithelial injury, while also generating reactive oxygen and nitrogen species capable of inducing genomic changes in vulnerable cycling or mitotically active epithelial cells in the proliferative zone.[19] Understanding the spectrum of immune

This is an open access article under the CC BY-NC-ND license (http://creativecommons.org/licenses/by-nc-nd/4.0/).

cell infiltrates and their interactions with mucosal epithelia may shed light on the underlying mechanisms of anti-PD-1-induced gastritis, further informing future clinical applications of immunotherapeutic agents.

We previously reported multiplexed ion beam imaging by time-of-flight (MIBI-TOF), a method that uses secondary ion mass spectrometry to image antibodies tagged with isotopically pure elemental metal reporters in formalin-fixed paraffin-embedded (FFPE) specimens.[20] This imaging technology can target multiple proteins on a single slide, circumventing the limitation imposed by insufficient sample availability. As the ion beam strikes the sample, monoisotopic elemental reporters conjugated to antibodies are liberated as secondary ions. These are measured and quantified by a TOF mass spectrometer. Thus, for each physical pixel in the tissue, a mass spectrum is recorded, representing the abundance of the antigens at that location.[20]

Here, we report a case of acute gastritis occurring in the setting of PD-1 inhibitor monotherapy. Using MIBI-TOF, we implemented a 28-plex imaging panel to identify the composition of inflammatory cells in gastric biopsies from a patient treated with anti-PD-1 immunotherapy.

RESULTS

Patient characteristics

The patient was a 53-year-old woman with a significant family history of colon cancer and uterine cancer, who initially presented in August 2014 with 2 years of progressive lower back pain. The clinical history of the patient is summarized in Figure 1A. At that time, she was found to have colorectal carcinoma and endometrial carcinoma, for which she underwent a right hemi-colectomy and total abdominal hysterectomy. The colon and endometrial tumors were morphologically and immunohistochemically distinct, representing two synchronous primary tumors. The colon tumor was a high-grade, advanced-stage (pT4bN1bM1b) adenocarcinoma, while the endometrial cancer was a focally high-grade International Federation of Gynecology and Obstetrics (FIGO) stage 1A endometrial carcinoma involving the upper endocervical mucosa with lymphovascular invasion. Genetic testing demonstrated heterozygosity for a putatively pathogenic MLH1 mutation (p.Q5242P), consistent with hereditary nonpolyposis colorectal cancer (HNPCC, Lynch syndrome). She was initially treated with 12 cycles of 5-fluorouracil, leucovorin, and oxaliplatin (mFOLFOX6) with avastin, as well as 3 treatments of high-dose brachytherapy to the vaginal cuff and canal. She tolerated her treatment well. Surveillance CT in November 2015 showed interval development of retroperitoneal adenopathy and left common iliac lymph node enlargement. Computed tomography (CT)-guided biopsy of a left retroperitoneal lymph node showed a metastatic, poorly/undifferentiated carcinoma with immunohistologic features supportive of endometrial origin.

She sought consultation at the University of California, Los Angeles (UCLA) in December 2015, where she received treatment with nivolumab (3 mg/kg intravenously [i.v.] every 2 weeks), given her history of Lynch syndrome and the promising results observed in patients with DNA mismatch repair deficiency treated with anti-PD-1.[21] She tolerated therapy well, with a partial response noted at 3 months, and complete response at 17 months. In August 2018, after 32 months of therapy with nivolumab, she developed severe epigastric pain, nausea, and anorexia. Endoscopic biopsy at that time demonstrated severely hyperemic gastric mucosa, which sloughed and bled readily. On histologic examination, random biopsies obtained from the body and antrum of the stomach showed diffuse eroded mucosa with crypt injury and dropout associated with intraepithelial and lamina propria mixed inflammation that included numerous neutrophils and lymphocytes, as well as scattered plasma cells, eosinophils, and mast cells (Figure 1B).

Nivolumab therapy was discontinued, and the patient received a high-dose oral steroid taper (prednisone), which led to the subsequent improvement of symptoms. Subsequent CT scans obtained 3.5 months after cessation of nivolumab therapy showed no evidence of active disease. The patient is being observed off therapy with serial CT scans.

Histological characteristics of gastric biopsies

To elucidate the main cell types involved in this dramatic clinical response, we analyzed biopsies of the inflammatory gastric antrum and body. Serial sections (4-μm-thick) were obtained for histological and multiplexed immunohistochemical examination. The biopsies from the gastric antrum and body showed similar features, which were characterized by diffusely eroded surface epithelium and infiltration of crypt epithelium by neutrophils and lymphocytes. Foci of more significant mucosal injury with crypt abscesses, crypt degeneration, and crypt dropout were noted. The lamina propria was diffusely expanded by mixed inflammatory infiltrates consisting of abundant lymphocytes, scattered plasma cells and neutrophils, and few eosinophils and mast cells (Figure 1B). Infection was excluded by a variety of special stains, including Grocott's methenamine silver (GMS) to exclude fungal organisms and further immunohistochemical stains that excluded cytomegalovirus, herpes simplex virus, Epstein-Barr virus, and *Helicobacter pylori* (Figure 1C). Biopsies from the esophagus and the first and second part of the duodenum were histologically unremarkable.

Multiparametric characterization of immune cellular infiltrates via MIBI-TOF

Gastric biopsies were obtained from the patient presented in this report as well as 8 controls that had no histological evidence of inflammation and no clinical history of gastritis. A total of 37 regions of interest (ROIs), 13 from the patient of interest, and the rest from controls, were selected based on the H&E stain and imaged using MIBI (Figures 2A and 2B). A serial section of gastric tissue was stained in parallel with tissue controls overnight using a single master mix of elementally labeled primary antibodies as previously described (Figures S1A and S1B; Table S1).[20] Twenty-eight MIBI markers were used to identify non-immune and immune cells along with functional markers (Figure 2C). Details related to marker localization in the tissue and image segmentation are shown in Figure 2D.

Segmented cell events were classified as mesenchymal (Mese), endothelial (Endo), stromal (SMC), epithelial (Epi), or

CellPress
OPEN ACCESS

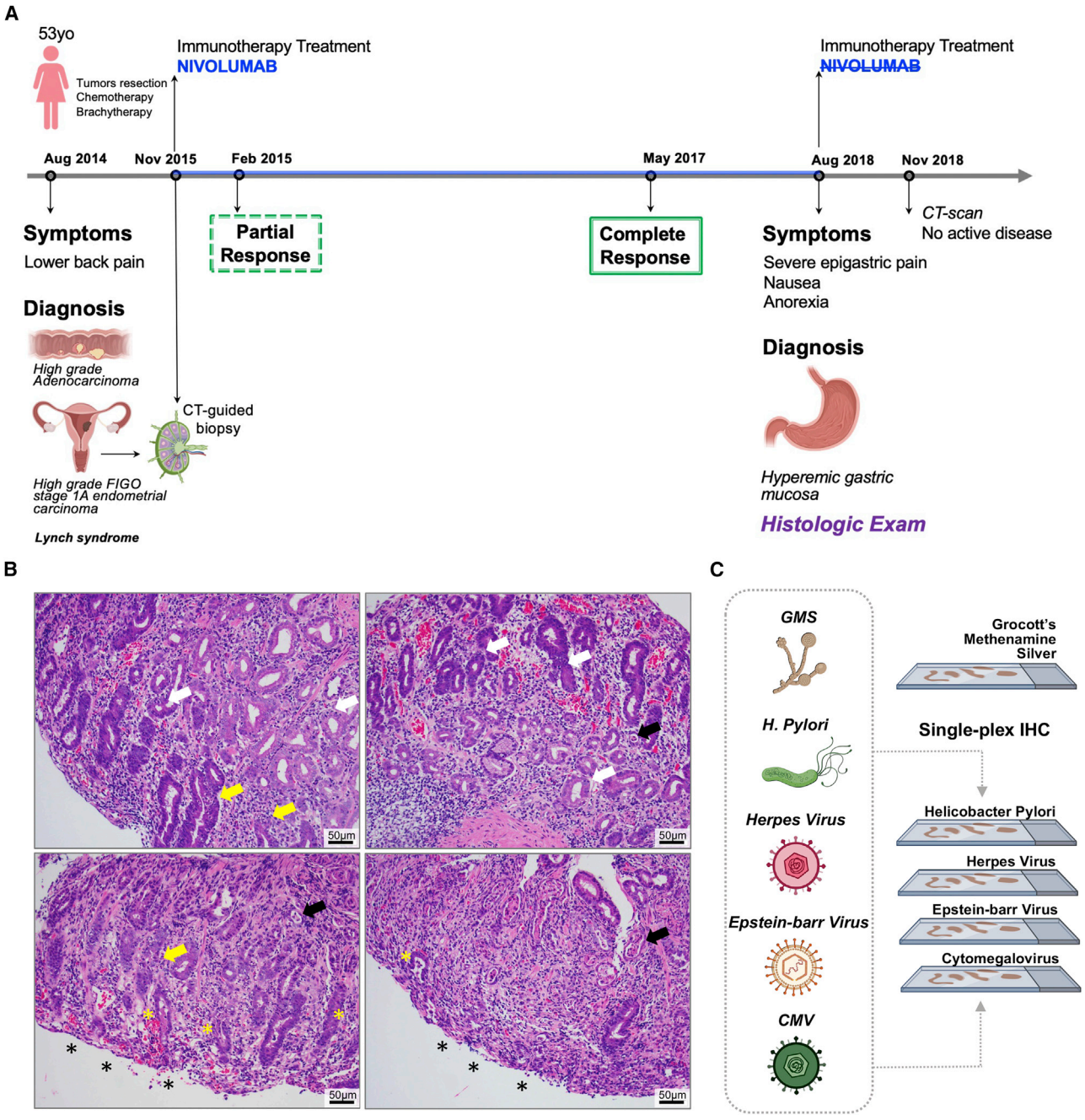

Figure 1. Clinical progression and histological features of immunotherapy-associated gastritis

(A) Scheme of the patient clinical progression. CT, computer tomography subjects; yo, years old.

(B) Representative hematoxylin and eosin (H&E) regions revealed diffusely eroded mucosa with variable infiltration of crypt epithelium by neutrophils (yellow arrows) or lymphocytes (white arrows) (top panels). Foci of more significant epithelial injury showing ulceration (black asterisks) with crypt abscesses (black arrows), crypt withering/degeneration (yellow asterisks), and crypt dropout were noted (bottom panels). The lamina propria across all biopsies was expanded by mixed inflammatory infiltrates consisting of abundant lymphocytes, scattered plasma cells and neutrophils, and few eosinophils and mast cells.

(C) Scheme of the special stains carried out to exclude infectious agents, including Grocott's methenamine silver (GMS) to exclude fungal organisms, and further immunohistochemical stains that excluded cytomegalovirus, herpes simplex virus, Epstein-Barr virus, and *Helicobacter pylori*.

immune based on area-normalized marker expression. Immune cells were further stratified into B cell (B cell), CD4 T cell (CD4 cell), CD8 T cell (CD8 cell), NK (natural killer) cell (NK), macrophage (Macro), monocyte (Mono), dendritic cell (DC), or mast cell (MCC) subsets. The expression profiles of key lineage markers across all subsets are shown in Figure 2E.

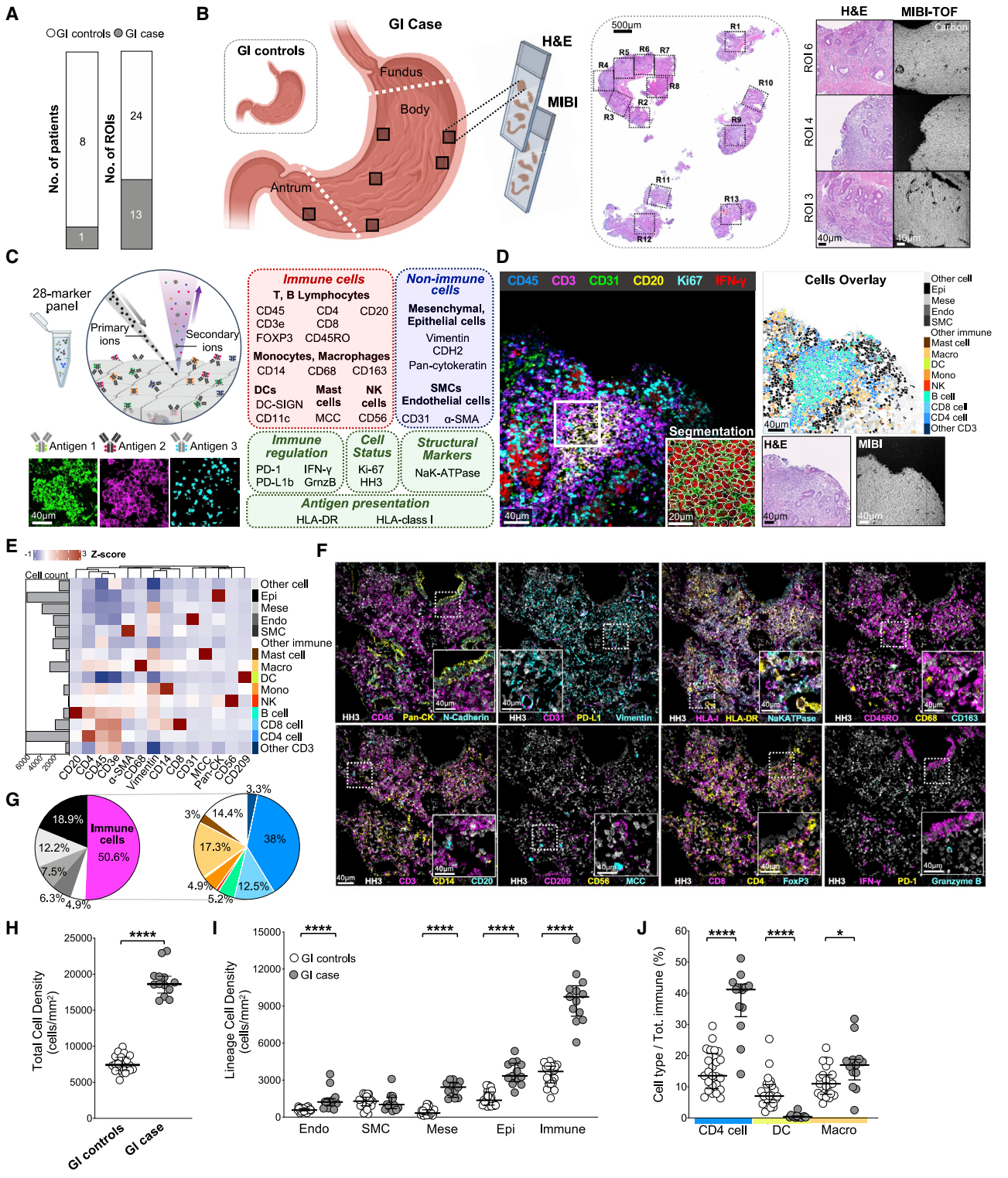

Figure 2. Multiplexed imaging interrogation of gastric biopsies after anti-PD-1 treatment

(A) Stacked barplot showing the number of patients profiled and regions of interest (ROIs) scanned for both healthy and diseased tissue.

(B) Representative image of the sampling approach for the study. Representative ROIs for the gastric biopsies were selected based on the H&E stain and rasterized with MIBI-TOF. The carbon channel from the MIBI-TOF scans reveal the structural similarity with the adjacent H&E section. The stomach image was created using BioRender.

(legend continued on next page)

Immune cells represented 50.6% of all cells found in the gastric tissue, followed by epithelium (18.9%), stroma (12.2%), endothelium (7.5%), and smooth muscle (6.3%). Approximately 5% of cells were negative for lineage-defining markers (categorized as Other Cells; Figures 2G and S1C). The majority of the immune cells were T lymphocytes (53.8%), followed by $CD68^{+}CD209^{-}$ macrophages (17.3%) and other immune cells (14.4%), while the remaining immune subsets each accounted for <5% (Figure 2G). A small portion of $CD45^{+}$ cells did not co-express other markers. Immune cell subsets compatible with this phenotype include plasma cells, neutrophils, or eosinophils. The majority of T cells were $CD4^{+}$ (70.7%) that expressed CD45RO, while a small fraction was $FOXP3^{+}$ regulatory T cells (4.2%). The majority of $CD8^{+}$ T cells lacked granzyme B (94.8%) and few T cells expressed PD-1. PD-L1 expression was infrequent and limited to a few epithelial cells.

With the exception of stromal cells, total cellularity and cell density were higher in the gastritis case compared with controls across cell lineages (Figures 2H and 2I). In addition, $CD4^{+}$ T cells and macrophages were increased, while DCs were decreased in the GI case compared to controls (Figures 2J, S1D, and S1E).

Interestingly, IFN-γ protein expression was sparsely found in T cells. Its expression was predominantly associated with glandular epithelial cells and a few bright cells within the lamina propria that co-expressed human leukocyte antigen-DR isotype (HLA-DR) and pan-cytokeratin (pan-CK) without CD45 or other immune markers (Figures 3A and 3B), suggesting that these bright IFN-γ^{+} cells were gastric/epithelial cells or $CD45^{-}$ neutrophils. IFN-γ^{+} gastric epithelial cells displayed high levels of Ki-67 across all regions (Figure 3C, short arrow). However, epithelial cells that were not proliferating did not express IFN-γ (Figure 3C, long arrow). Quantitative analyses further supported the notion that IFN-γ expression was predominantly associated with epithelial cells (Figures 3D and S1F). Indeed, 80.7% of epithelial cells expressed IFN-γ. These findings were subsequently confirmed by *in situ* hybridization (ISH) in a serial tissue section. The experimental approach to validate mRNA IFN-γ detection in gastric tissue is summarized in Figure S2A. Assay control along with IFN-γ controls in FFPE tissue microarrays were performed in parallel with the gastric biopsy for the detection of IFN-γ transcript by single-plex ISH (Figure S2B). Single-plex immunohistochemistry (IHC) was performed on a serial section of the tissue microarrays to confirm the results. Scattered cells expressed IFN-γ transcript in normal tonsil tissue. These cells, probably lymphocytes, were not found in the serial section obtained for single-plex IHC. A correlation between IFN-γ protein and transcript was observed in ductal carcinoma *in situ* (DCIS) tissue. Lastly, the absence of IFN-γ transcript, despite the presence of protein, was observed in lung adenocarcinoma, possibly due to RNA degradation or the absence of ongoing transcription. These results were further corroborated by MIBI-TOF, overlaying several immune markers with IFN-γ in tissue controls (data not shown) to confirm the expression of IFN-γ by immune cells. Our results in the gastric biopsy revealed that IFN-γ mRNA was limited to gastric epithelial cells and a few bright cells within the lamina propria (Figure 3E). In contrast, normal stomach biopsy showed scattered IFN-γ mRNA associated with immune cells (Figure S2C). Furthermore, proximal sections of the gastric specimen analyzed by MIBI-TOF and ISH-mRNA confirmed that IFN-γ producing epithelial cells displayed elevated Ki-67 expression (Figure S2D).

The salient features in this case study of PD-1 blockade-associated gastritis include lamina propria expansion by mononuclear inflammation characterized mainly by T lymphocytes, epithelial injury from crypt apoptosis, intraepithelial lymphocytic and neutrophilic inflammation, and IFN-γ production by gastric epithelial cells.

DISCUSSION

Here, we examined a case of acute gastritis occurring in the setting of PD-1 inhibitor monotherapy in a patient with a history of Lynch syndrome. Endoscopic observation demonstrated severely hyperemic gastric mucosa accompanied by sloughing and bleeding. On pathologic examination, biopsy tissue contained diffusely eroded mucosa and crypt injury that was accompanied by expansion of the lamina propria due to the infiltration of neutrophils and mature lymphocytes. Subsequent 28-plex imaging found this infiltrate to comprise predominantly CD4 and CD8 T lymphocytes, with few regulatory T cells and sparse expression of PD-1. Lastly, the gastric epithelium had upregulated IFN-γ.

(C) Overview of the MIBI-TOF workflow and panel. MCC, mast cell chymase; CDH2, N-cadherin; α-SMA, alpha-smooth muscle actin; GrnzB, Granzyme B; HH3, histone H3; HLA-DR, human leukocyte antigen – DR isotype; HLA-class I, human leukocyte antigen class I.

(D) Representative marker overlay from a gastric tissue section selected based on paired H&E, along with the MIBI-TOF workflow for segmentation and downstream analyses. Epi, epithelial cell; Mese, mesenchymal cell; Endo, endothelial cell; SMC, smooth muscle cell/myofibroblast; Macro, macrophage; Mono, monocyte; NK, natural killer (NK) cell; H&E, hematoxylin and eosin (H&E) stain.

(E) Cell lineage assignments based on normalized expression of lineage markers (heatmap columns). Columns are hierarchically clustered (Euclidean distance, average linkage), while rows are ordered by cell lineage (top) and immune cell breakdown (bottom). A bar plot with the absolute abundance of each cell type is displayed (left).

(F) Localization of 25 different markers within a representative MIBI image of a gastric tissue section. A 4-color overlay of lineage-specific and functional markers is shown per image.

(G) Pie charts displaying the proportion of immune, epithelial, and endothelial cells and other lineage-specific markers over the total cells and across all regions (left); and the proportion of different immune cell subsets within the total $CD45^{+}$ cells (right). HH3, histone H3; Pan-CK, pan-cytokeratin; HLA-I, human leukocyte antigen class I; MCC, mast cell chymase; Vim, vimentin.

(H) Scatterplot depicting the total cell density (cell/mm^2) per ROI for healthy and diseased gastric tissues.

(I) Scatterplot depicting the lineage cell density (cell/mm^2) per ROI for healthy and diseased gastric tissues.

(J) Frequency of immune cell subsets of total immune cells. Lines represent the median and interquartile range (IQR). All p values calculated with a Wilcoxon rank-sum test, where ns $p > 0.05$, *$p < 0.05$, **$p < 0.01$, ***$p < 0.001$.

See also Figure S1.

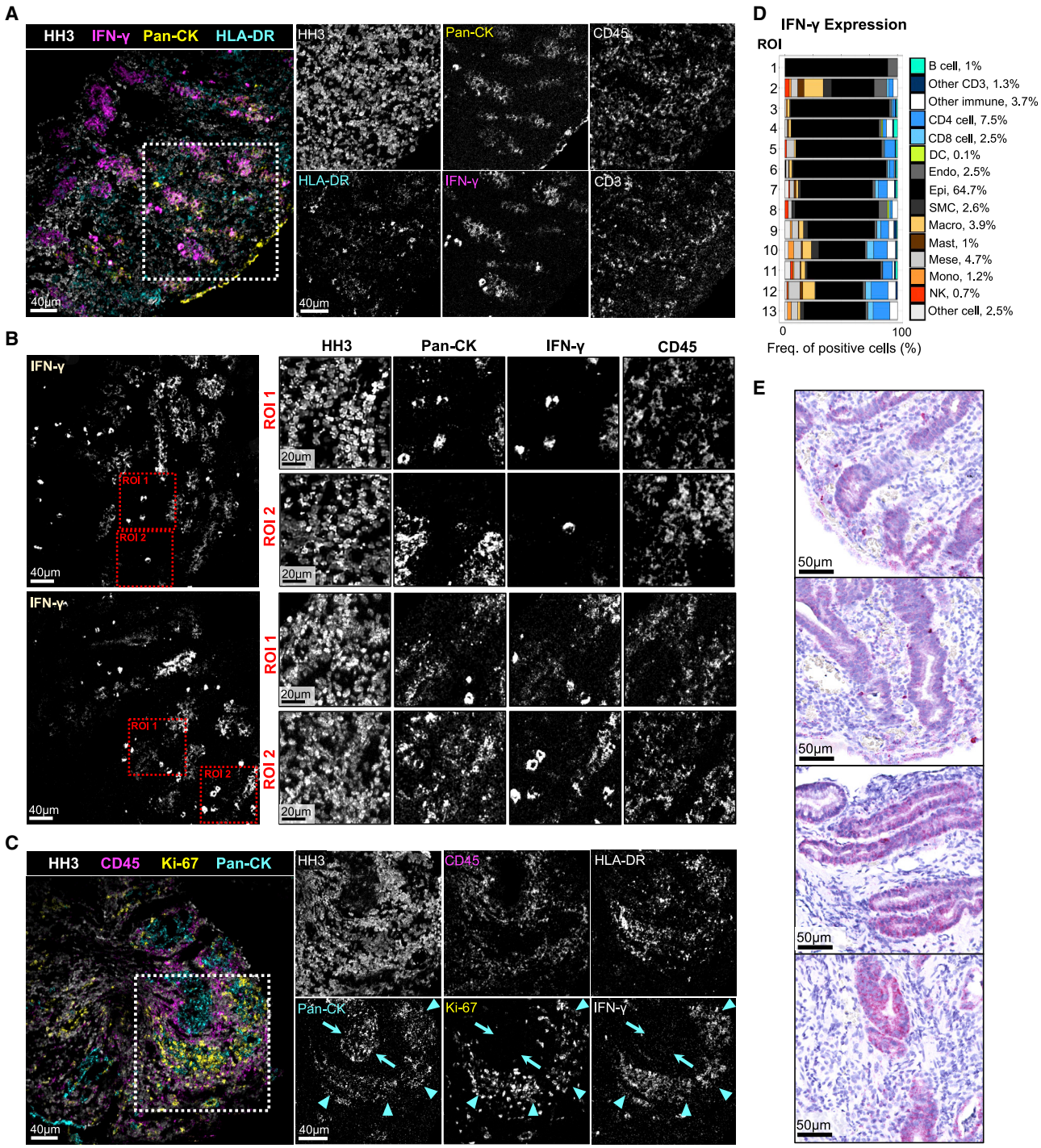

Figure 3. IFN-γ producing, hyperproliferative gastric epithelial cells using MIBI-TOF

(A) Color overlay of IFN-γ$^+$ cells (magenta), pan-CK$^+$ epithelial cells (yellow), and major histocompatibility complex (MHC) class II cells (light blue) in a representative region of gastric biopsy, accompanied by CD45 and CD3 expression in the same region.

(B) Localization of IFN-γ protein in 2 different representative regions of gastric biopsies (left). Random areas with IFN-γ$^+$ cells were selected and expression of pan-CK, IFN-γ, and CD45 is displayed (right).

(C) Color overlay of CD45$^+$ pan-leukocyte marker (magenta), Ki-67$^+$ proliferating cells (yellow), and pan-CK$^+$ epithelial cells (light blue) in a representative region of gastric biopsy, accompanied by MHC class II and IFN-γ expression in the same region. Light blue arrows signify the presence (shorter arrow) or absence (longer arrow) of IFN-γ and Ki-67 co-expression in epithelial cells.

(legend continued on next page)

Several studies have reported that cytokine production by Th1, Th17, and Th2 cells can induce gastritis and oxyntic injury in the setting of gastric cancer and *H. pylori*-induced gastritis.[16,17] In this case study, IFN-γ expression was predominantly found in the epithelial cells, and to a lesser extent in T cells (Figures 3A and S1F). However, considering that >50% of the immune cells found within the gastric biopsy were T cells, one possible explanation for gastritis under these conditions is that other soluble mediators, such as tumor necrosis factor-α (TNF-α),[22] IL-17, or a skewed type 2 immune response may have contributed to the induction of disease.[16] In line with our results, combination therapy of nivolumab and IFN-γ was reported to have the greatest effect on PD-1 blockade, compared with IFN-γ or nivolumab alone.[23] In addition, constitutive PD-1 expression constitutes a form of immune adaptation to chronic stimulation, limiting immune responses and preventing autoimmune phenomena. In the absence of PD-1, T cell priming is observed instead of tolerance, supporting the view that PD-1 plays a role in maintaining tolerance.[24] Consistent with this, our results indicate that prolonged anti-PD-1 treatment and IFN-γ secretion may downregulate PD-1 expression on T cells, resulting in T cell activation and induction of soluble mediators.

IFN-γ has been shown to induce gastritis and oxyntic atrophy.[16,17] However, epithelial cells secreting inflammatory cytokines that may regulate gastritis are rarely reported.[18] Our results demonstrate epithelial IFN-γ overproduction accompanied by heightened proliferation of the gastric epithelia. Epithelial damage in the context of chronic gastritis results in accelerated exfoliation and cell death. The gastric mucosa responds to this insult by increasing the number of cells produced in the proliferative compartment, which then migrate luminally to replace the lost cells.[25] Furthermore, previous studies of colon biopsy samples from patients with immune checkpoint blockade-induced colitis typically reveal a mixed lymphocytic and neutrophilic infiltrate (without accompanying plasma cells or eosinophils) with apoptotic mucosal epithelial cells and crypt abscesses.[26] However, the structure of the epithelium is usually preserved, in contrast to the pathology of IBD.

The epithelial proliferation found in this study is consistent with ongoing regeneration in response to significant injury and loss of mucosal integrity in the form of both surface and crypt epithelial damage (Figure 3C). This increase in proliferative activity was noticed across the biopsy with expansion of the proliferative zone and increased IFN-γ secretion. In addition, histopathological analyses revealed crypt apoptosis and eroded mucosa with variable infiltration of the crypt epithelium by neutrophils (Figure 1B). These results are consistent with the contribution of mitotically active gastric epithelial cells to the observed gastritis, in which the inflammatory phenotype evoked from PD-1 blockade may induce rapid, compensatory cell turnover previously observed in models of *H. pylori* gastritis.[25,27]

This landscape could be explained by one or both of the following mechanisms. First, the loss of mucosal integrity may allow stomach contents to penetrate beyond the gastric epithelium. Gastric acids can cause bleeding and perforation by compromising gastric epithelial integrity and triggering local inflammatory responses.[28] Second, this may be due to neutrophils selectively infiltrating the proliferative zones while sparing surface and deep glandular zones.[19] Previous work has shown that, in some cases, neutrophils may infiltrate surface zones, where they can form pit abscesses.[19]

To conclude, the histopathology and cellular composition found here, in conjunction with the clinical resolution of symptoms upon cessation of nivolumab therapy, are consistent with anti-PD-1-induced gastritis. Although steroid therapy is reportedly effective in most cases of immune checkpoint inhibitor-induced gastritis, a few cases have also required immunosuppressive agents.[29] Thus, additional investigation to increase our understanding of the regulation of inflammation and epithelial cell changes in the upper GI tract after PD-1 therapy are needed to inform future immunotherapy strategies.

Limitations of the study

This study has some limitations. Although we observed neutrophils in the histologic study, in-depth profiling of this cell type would help us to better understand the contribution of neutrophil-associated inflammation to gastric oxidative stress and injury induced by anti-PD-1 treatment. Further markers showing epithelial integrity and apoptosis may have helped to generate further hypotheses regarding gastric epithelial cell proliferation in response to increased apoptosis. These findings should be investigated further, including a larger cohort of patients with gastritis induced by other agents (*H. pylori*, nonsteroidal anti-inflammatory drugs, or different immune checkpoint inhibitors), along with *in vitro* assays to support the proposed mechanism highlighted by our MIBI findings.

STAR★METHODS

Detailed methods are provided in the online version of this paper and include the following:

- KEY RESOURCES TABLE
- RESOURCE AVAILABILITY
  - Lead contact
  - Materials availability
  - Data and code availability
- EXPERIMENTAL MODEL AND SUBJECT DETAILS
- METHOD DETAILS
  - Histological and MIBI-TOF studies
  - Antibody preparation
  - Tissue staining
  - Tissue controls and antibody validation
  - MIBI-TOF imaging
  - *In situ* hybridization studies
- QUANTIFICATION AND STATISTICAL ANALYSIS

(D) Stacked bars depicting the relative abundance of IFN-γ $^{+}$ cells across all ROIs and cell types.
(E) *In situ* hybridization in a serial gastric tissue section. Four representative regions are displayed.
HH3, histone H3; Pan-CK, pan-cytokeratin.
See also Figure S2.

- Single-cell segmentation
- Dataset normalization and clustering
- Statistical analyses
- Software

SUPPLEMENTAL INFORMATION

Supplemental information can be found online at https://doi.org/10.1016/j.xcrm.2021.100419.

ACKNOWLEDGMENTS

M.A. is supported by NIH 1-DP5-OD019822. S.C.B. and M.A. are supported by NIH 1R01AG056287-01, 1R01AG057915-01, and 1U24CA224309-01; the Bill and Melinda Gates Foundation; and a Translational Research Award from the Stanford Cancer Institute. S.C.B. is supported by a gift from Christy and Bill Neidig, the Damon Runyon Cancer Research Foundation (DRG-2017-09), and NIH 1DP2OD022550-01, 1-R00-GM104148-01, 5U19AI116484-02, and U19 AI104209. The Stanford Nano Shared Facility is supported by NSF ECCS-1542152. C.C.L. was supported by the Stanford Graduate Fellowship. E.F.M. was supported by the NSF Graduate Research Fellowship (grant no. 2017242837) and NIH 5T32AI007290. T.S.N. is supported by NIH/NCI grant 1K08CA241088 and the Hyundai Hope on Wheels Young Investigator Award.

AUTHOR CONTRIBUTIONS

S.F. conceived the study design, performed the experiments, analyzed the data, and wrote the manuscript; T.S.N. assisted with drafting the manuscript; C.C.L. implemented the image segmentation and assisted with data analysis; E.F.M. and R.K. assisted with assay development and performed the experiments; A.B. assisted with image processing; D.W.D., J.A.G., A.R., and S.C.B. assisted with reviewing and editing of the manuscript; M.A. supervised the work.

DECLARATION OF INTERESTS

S.F. was a paid speaker for an IonPath webinar. M.A. and S.C.B. have patents relating to MIBI technology and are paid consultants and shareholders at IonPath. E.F.M. has previously consulted for IonPath.

Received: February 29, 2020
Revised: June 21, 2021
Accepted: September 22, 2021

REFERENCES

1. Buchbinder, E.I., and Desai, A. (2016). CTLA-4 and PD-1 pathways: similarities, differences, and implications of their inhibition. Am. J. Clin. Oncol. *39*, 98–106.
2. Keir, M.E., Butte, M.J., Freeman, G.J., and Sharpe, A.H. (2008). PD-1 and its ligands in tolerance and immunity. Annu. Rev. Immunol. *26*, 677–704.
3. Hofmann, L., Forschner, A., Loquai, C., Goldinger, S.M., Zimmer, L., Ugurel, S., Schmidgen, M.I., Gutzmer, R., Utikal, J.S., Göppner, D., et al. (2016). Cutaneous, gastrointestinal, hepatic, endocrine, and renal side-effects of anti-PD-1 therapy. Eur. J. Cancer *60*, 190–209.
4. Larkin, J., Chiarion-Sileni, V., Gonzalez, R., Grob, J.J., Cowey, C.L., Lao, C.D., Schadendorf, D., Dummer, R., Smylie, M., Rutkowski, P., et al. (2015). Combined nivolumab and ipilimumab or monotherapy in untreated melanoma. N. Engl. J. Med. *373*, 23–34.
5. McDermott, D.F., Sosman, J.A., Sznol, M., Massard, C., Gordon, M.S., Hamid, O., Powderly, J.D., Infante, J.R., Fassò, M., Wang, Y.V., et al. (2016). Atezolizumab, an anti-programmed death-ligand 1 antibody, in metastatic renal cell carcinoma: long-term safety, clinical activity, and immune correlates from a phase Ia study. J. Clin. Oncol. *34*, 833–842.
6. Balar, A.V., Galsky, M.D., Rosenberg, J.E., Powles, T., Petrylak, D.P., Bellmunt, J., Loriot, Y., Necchi, A., Hoffman-Censits, J., Perez-Gracia, J.L., et al.; IMvigor210 Study Group (2017). Atezolizumab as first-line treatment in cisplatin-ineligible patients with locally advanced and metastatic urothelial carcinoma: a single-arm, multicentre, phase 2 trial. Lancet *389*, 67–76.
7. Collins, M., Michot, J.M., Danlos, F.X., Mussini, C., Soularue, E., Mateus, C., Loirat, D., Buisson, A., Rosa, I., Lambotte, O., et al. (2017). Inflammatory gastrointestinal diseases associated with PD-1 blockade antibodies. Ann. Oncol. *28*, 2860–2865.
8. Gonzalez, R.S., Salaria, S.N., Bohannon, C.D., Huber, A.R., Feely, M.M., and Shi, C. (2017). PD-1 inhibitor gastroenterocolitis: case series and appraisal of 'immunomodulatory gastroenterocolitis'. Histopathology *70*, 558–567.
9. Lu, J., Firpi-Morell, R.J., Dang, L.H., Lai, J., and Liu, X. (2018). An unusual case of gastritis in one patient receiving PD-1 blocking therapy: coexisting immune-related gastritis and cytomegaloviral infection. Gastroenterol. Res. *11*, 383–387.
10. Topalian, S.L., Hodi, F.S., Brahmer, J.R., Gettinger, S.N., Smith, D.C., McDermott, D.F., Powderly, J.D., Carvajal, R.D., Sosman, J.A., Atkins, M.B., et al. (2012). Safety, activity, and immune correlates of anti-PD-1 antibody in cancer. N. Engl. J. Med. *366*, 2443–2454.
11. Hamid, O., Robert, C., Daud, A., Hodi, F.S., Hwu, W.-J., Kefford, R., Wolchok, J.D., Hersey, P., Joseph, R.W., Weber, J.S., et al. (2013). Safety and tumor responses with lambrolizumab (anti-PD-1) in melanoma. N. Engl. J. Med. *369*, 134–144.
12. Boike, J., and Dejulio, T. (2017). Severe esophagitis and gastritis from nivolumab therapy. ACG Case Rep. J. *4*, e57.
13. Hayama, N., Ihara, H., Honma, Y., Itoigawa, Y., Kaira, K., and Fujii, M. (2020). Severe gastritis due to pembrolizumab treatment in a lung cancer patient. Respirol. Case Rep. *8*, e00636.
14. DiPaolo, R.J., Glass, D.D., Bijwaard, K.E., and Shevach, E.M. (2005). CD4+CD25+ T cells prevent the development of organ-specific autoimmune disease by inhibiting the differentiation of autoreactive effector T cells. J. Immunol. *175*, 7135–7142.
15. DiPaolo, R.J., Brinster, C., Davidson, T.S., Andersson, J., Glass, D., and Shevach, E.M. (2007). Autoantigen-specific TGFbeta-induced Foxp3+ regulatory T cells prevent autoimmunity by inhibiting dendritic cells from activating autoreactive T cells. J. Immunol. *179*, 4685–4693.
16. Stummvoll, G.H., DiPaolo, R.J., Huter, E.N., Davidson, T.S., Glass, D., Ward, J.M., and Shevach, E.M. (2008). Th1, Th2, and Th17 effector T cell-induced autoimmune gastritis differs in pathological pattern and in susceptibility to suppression by regulatory T cells. J. Immunol. *181*, 1908–1916.
17. Huter, E.N., Stummvoll, G.H., DiPaolo, R.J., Glass, D.D., and Shevach, E.M. (2009). Pre-differentiated Th1 and Th17 effector T cells in autoimmune gastritis: Ag-specific regulatory T cells are more potent suppressors than polyclonal regulatory T cells. Int. Immunopharmacol. *9*, 540–545.
18. Bockerstett, K.A., and DiPaolo, R.J. (2017). Regulation of gastric carcinogenesis by inflammatory cytokines. Cell. Mol. Gastroenterol. Hepatol. *4*, 47–53.
19. Lee, I. (2014). Critical pathogenic steps to high risk Helicobacter pylori gastritis and gastric carcinogenesis. World J. Gastroenterol. *20*, 6412–6419.
20. Keren, L., Bosse, M., Marquez, D., Angoshtari, R., Jain, S., Varma, S., Yang, S.-R., Kurian, A., Van Valen, D., West, R., et al. (2018). A Structured Tumor-Immune Microenvironment in Triple Negative Breast Cancer Revealed by Multiplexed Ion Beam Imaging. Cell *174*, 1373–1387.e19.
21. Le, D.T., Uram, J.N., Wang, H., Bartlett, B.R., Kemberling, H., Eyring, A.D., Skora, A.D., Luber, B.S., Azad, N.S., Laheru, D., et al. (2015). PD-1 blockade in tumors with mismatch-repair deficiency. N. Engl. J. Med. *372*, 2509–2520.

22. Hasegawa, S., Nishikawa, S., Miura, T., Saito, Y., Madarame, H., Sekikawa, K., Tagawa, Y., Iwakura, Y., and Nakane, A. (2004). Tumor necrosis factor-α is required for gastritis induced by Helicobacter felis infection in mice. Microb. Pathog. *37*, 119–124.

23. Ding, G., Shen, T., Yan, C., Zhang, M., Wu, Z., and Cao, L. (2019). IFN-γ down-regulates the PD-1 expression and assist nivolumab in PD-1-blockade effect on CD8+ T-lymphocytes in pancreatic cancer. BMC Cancer *19*, 1053.

24. Probst, H.C., McCoy, K., Okazaki, T., Honjo, T., and van den Broek, M. (2005). Resting dendritic cells induce peripheral CD8+ T cell tolerance through PD-1 and CTLA-4. Nat. Immunol. *6*, 280–286.

25. Lynch, D.A., Mapstone, N.P., Clarke, A.M., Jackson, P., Moayyedi, P., Dixon, M.F., Quirke, P., and Axon, A.T. (1999). Correlation between epithelial cell proliferation and histological grading in gastric mucosa. J. Clin. Pathol. *52*, 367–371.

26. Martins, F., Sofiya, L., Sykiotis, G.P., Lamine, F., Maillard, M., Fraga, M., Shabafrouz, K., Ribi, C., Cairoli, A., Guex-Crosier, Y., et al. (2019). Adverse effects of immune-checkpoint inhibitors: epidemiology, management and surveillance. Nat. Rev. Clin. Oncol. *16*, 563–580.

27. Yoshimura, T., Shimoyama, T., Tanaka, M., Sasaki, Y., Fukuda, S., and Munakata, A. (2000). Gastric mucosal inflammation and epithelial cell turnover are associated with gastric cancer in patients with Helicobacter pylori infection. J. Clin. Pathol. *53*, 532–536.

28. Souza, R.F., Huo, X., Mittal, V., Schuler, C.M., Carmack, S.W., Zhang, H.Y., Zhang, X., Yu, C., Hormi-Carver, K., Genta, R.M., and Spechler, S.J. (2009). Gastroesophageal reflux might cause esophagitis through a cytokine-mediated mechanism rather than caustic acid injury. Gastroenterology *137*, 1776–1784.

29. Johncilla, M., Grover, S., Zhang, X., Jain, D., and Srivastava, A. (2020). Morphological spectrum of immune check-point inhibitor therapy-associated gastritis. Histopathology *76*, 531–539.

30. Greenwald, N.F., Miller, G., Moen, E., Kong, A., Kagel, A., Fullaway, C.C., McIntosh, B.J., Leow, K., Schwartz, M.S., Dougherty, T., et al. (2021). Whole-cell segmentation of tissue images with human-level performance using large-scale data annotation and deep learning. bioRxiv. https://doi.org/10.1101/2021.03.01.431313.

31. Van Gassen, S., Callebaut, B., Van Helden, M.J., Lambrecht, B.N., Demeester, P., Dhaene, T., and Saeys, Y. (2015). FlowSOM: using self-organizing maps for visualization and interpretation of cytometry data. Cytometry A *87*, 636–645.

STAR★METHODS

KEY RESOURCES TABLE

REAGENT or RESOURCE	SOURCE	IDENTIFIER
Antibodies		
Histone H3 (Clone D1H2)	Cell Signaling Technology	Cat#4499BF; RRID: AB_10544537
Vimentin (Clone D21H3)	Cell Signaling Technology	Cat#5741BF; RRID: AB_10695459
Smooth Muscle Actin (Clone SP151)	Spring	Cat#M4714.C; RRID: N/A
Granzyme B (Clone D6E9W)	Cell Signaling Technology	Cat#46890BF; RRID: AB_2799313
CD4 (Clone EPR6855)	AbCam	Cat#ab181724; RRID: N/A
CD14 (Clone D7A2T)	Cell Signaling Technology	Cat#56082BF; RRID: AB_2799504
CD56 (Clone MRQ-42)	Cell Marque	Cat#156R-9-OEM; RRID: N/A
FoxP3 (Clone 236A/E7)	BD Biosciences	Cat#624084; RRID: N/A
PD-1 (Clone D4W2J)	Cell Signaling Technology	Cat# 86163BF; RRID: AB_2728833
CD31 (Clone EP3095)	AbCam	Cat#ab216459; RRID: N/A
PD-L1 biotinylated (Clone E1L3N)	Cell Signaling Technology	Cat#15118S; RRID: AB_2798715
Biotin (Clone 1D4-C5)	Biolegend	Cat#409002; RRID: AB_10642032
Ki67 (Clone 8D5)	Cell Signaling Technology	Cat#9449BF; RRID: N/A
DC-SIGN (Clone DCN46)	BD Biosciences	Cat#624084; RRID: N/A
CD163 (Clone EPR19518)	AbCam	Cat#ab213731; RRID: N/A
CD68 (Clone D4B9C)	Cell Signaling Technology	Cat#76437BF; RRID: AB_2799882
CD8 (Clone C8/144B)	Cell Marque	Cat#108M-94; RRID: AB_1158205
CD3e (Clone D7A6E)	Cell Signaling Technology	Cat#85061BF; RRID: N/A
CD11c (Clone EP1347Y)	AbCam	Cat#ab216655; RRID: N/A
CD45RO (Clone UCHL1)	Biolegend	Cat#304202; RRID: AB_314418
CD20 (Clone L26)	Cell Marque	Cat#120M-84; RRID: AB_1158145
IFN-γ (Clone IFNG/466)	AbCam	Cat#ab218890; RRID: N/A
HLA-DR (Clone EPR3692)	AbCam	Cat#ab215985; RRID: N/A
CD45 (Clone D9M8I)	Cell Signaling Technology	Cat#13917BF; RRID: AB_2750898
Pan-cytokeratin (Clone AE1/AE3)	ThermoFisher	Cat#MS-343-PABX; RRID: AB_61537
Mast Cell Chymase (Clone EPR13136)	AbCam	Cat#ab233729; RRID: N/A
N-Cadherin (Clone 5D5)	AbCam	Cat#ab98952; RRID: AB_10696943
NaK ATPase (Clone EP1845Y)	AbCam	Cat#ab167390; RRID: N/A
HLA Class I (Clone EMR8-5)	AbCam	Cat#ab70328; RRID: AB_1269092
Biological samples		
Gastric biopsies from carcinoma patient and eight controls (tissue with no histological evidence of inflammation and no clinical history of gastritis)	N/A	N/A
Chemicals, peptides, and recombinant proteins		
TBS IHC Wash Buffer with Tween 20	Cell Marque	Cat#935B-09
PBS IHC Wash Buffer with Tween 20	Cell Marque	Cat#934B-09
Target Retrieval Solution, pH 9, (3:1)	Agilent (Dako)	Cat#S2375
Avidin/Biotin Blocking Kit	Biolegend	Cat#927301
Gelatin (cold water fish skin)	Sigma-Aldrich	Cat#G7765-250
Xylene Histological grade	Sigma-Aldrich	Cat#534056-500
Glutaraldehyde 8% Aqueous Solution EM Grade	EMS	Cat#16020
Normal Donkey serum	Sigma-Aldrich	Cat#D9663-10ML

(*Continued on next page*)

CellPress
OPEN ACCESS

Continued

REAGENT or RESOURCE	SOURCE	IDENTIFIER
Bovine Albumin (BSA)	Fisher	Cat#BP1600-100
Centrifugal filters (0.1 μm)	Millipore	Cat#UFC30VV00
RNAscope® Hydrogen Peroxide solution	ACDBio	Cat#322335
RNAscope® Target retrieval solution	ACDBio	Cat#322000
Critical commercial assays		
Maxpar X8 Antibody labeling kit	Fluidigm	Cat#2011XXX
MIBItag Conjugation Kit	IonPath	Cat#600XXX
ImmPRESS UNIVERSAL (Anti-Mouse/Anti-Rabbit) IgG KIT (HRP)	Vector Laboratories	Cat#MP-7500-15
ImmPACT DAB (For HRP Substrate)	Vector Laboratories	Cat#SK-4105
RNAscope® 2.5 HD Reagent Kit-Red	ACDBio	Cat#322360
RNAscope® 2.5 HD Reagent Kit-Brown	ACDBio	Cat#322310
Deposited data		
MIBI-TOF images, segmentation output, cell phenotype maps, and extracted cell tables	This paper	Zenodo:
Oligonucleotides		
RNAscope® Probe Hs-IFNG	ACDBio	Cat#310501
RNAscope® Positive Control Probe Hs-PPIB	ACDBio	Cat#313901
RNAscope® Negative Control Probe	ACDBio	Cat#310043
RNAscope® Hs-UBC	ACDBio	Cat#5101512
Software and algorithms		
MATLAB 2019a	Mathworks	N/A
Mesmer cell segmentation tool	Greenwald et al., 2021[30]	https://www.deepcell.org/predict
Analysis code	This paper	Zenodo: https://zenodo.org/record/5500734

RESOURCE AVAILABILITY

Lead contact

Further information and requests for resources and reagents should be directed to and will be fulfilled by the lead contact, Michael Angelo (mangelo0@stanford.edu).

Materials availability

This study did not generate new unique reagents.

Data and code availability

Imaging data have been deposited at Zenodo and are publicly available as of the date of publication. DOIs are listed in the Key resources table.

All original code has been deposited at Zenodo and is publicly available as of the date of publication. DOIs are listed in the Key resources table.

Any additional information required to reanalyze the data reported in this paper is available from the lead contact upon request.

EXPERIMENTAL MODEL AND SUBJECT DETAILS

Human samples were acquired in accordance with IRB protocol #46646. We analyzed gastric biopsies of a carcinoma patient (53 years old, female) and 8 controls (histologically normal and untreated, tissue with no histological evidence of inflammation and no clinical history of gastritis) (age: 19-53, 7 males and 1 female) using MIBI-TOF. Stanford University oversaw this work.

METHOD DETAILS

Histological and MIBI-TOF studies

Serial sections (4 μm thickness) were obtained for histological and immunohistochemical examination (Figure 2B). Clinical FFPE tissue specimen in parallel with tissue controls for each marker were placed on gold slides and stained overnight using a single master mix comprised of elementally-labeled primary antibodies (Figures S1A and S1B; Table S1). All targets were stained together without the need for cyclical steps or enzymatic reactions as previously described.[20] Thirteen representative regions of interest for the case study and twenty-four regions of interest for the respective normal GI controls were selected based on the H&E stain and rasterized (Figures 2A and 2B).

Antibody preparation

Antibodies were conjugated to isotopic metal reporters as described previously.[20] Following conjugation, antibodies were diluted in Candor PBS Antibody Stabilization solution (Candor Bioscience). Antibodies were either stored at 4°C or lyophilized in 100 mM D-(+)-Trehalose dehydrate (Sigma Aldrich) with ultrapure distilled H2O for storage at −20°C. Prior to staining, lyophilized antibodies were reconstituted in a buffer of Tris (Thermo Fisher Scientific), sodium azide (Sigma Aldrich), ultrapure water (Thermo Fisher Scientific), and antibody stabilizer (Candor Bioscience) to a concentration of 0.05 mg/mL.

Tissue staining

Slides were baked at 70°C overnight followed by deparaffinization and rehydration with washes in xylene (3x), 100% ethanol (2x), 95% ethanol (2x), 80% ethanol (1x), 70% ethanol (1x), and ddH2O with a Leica ST4020 Linear Stainer (Leica Biosystems). Tissues next underwent antigen retrieval by submerging sides in 3-in-1 Target Retrieval Solution (pH 9, DAKO Agilent) and incubating at 97°C for minutes in a Lab Vision PT Module (Thermo Fisher Scientific). After cooling to room temperature slides were washed in 1x PBS IHC Washer Buffer with Tween 20 (Cell Marque) with 0.1% (w/v) bovine serum albumin (Thermo Fisher). Next, all tissues underwent two rounds of blocking, the first to block endogenous biotin and avidin with an Avidin/Biotin Blocking Kit (Biolegend). Tissues were then washed with wash buffer and blocked for 1 h at room temperature with 1x TBS IHC Wash Buffer with Tween 20 with 3% (v/v) normal donkey serum (Sigma-Aldrich), 0.1% (v/v) cold fish skin gelatin (Sigma Aldrich), 0.1% (v/v) Triton X-100, and 0.05% (v/v) sodium azide. The antibody cocktail was prepared in 1x TBS IHC Wash Buffer with Tween 20 with 3% (v/v) normal donkey serum (Sigma-Aldrich) and filtered through a 0.1 μm centrifugal filter (Millipore) prior to incubation with tissue overnight at 4°C in a humidity chamber. Following the overnight incubation slides were washed twice for 5 min in wash buffer and fixed in a solution of 2% glutaraldehyde (Electron Microscopy Sciences) solution in low-barium PBS for 5 min. Slides were washed in PBS (1x), 0.1 M Tris at pH 8.5 (3x), ddH2O (2x), and then dehydrated by washing in 70% ethanol (1x), 80% ethanol (1x), 95% ethanol (2x), and 100% ethanol (2x). Slides were dried under vacuum prior to imaging.

Tissue controls and antibody validation

Testing appropriate tissue sets to determine analytic sensitivity and specificity is part of the MIBI validation assay as described in our previous publication.[20] Appropriate positive and negative tissue controls were selected and compiled into a tissue microarray (TMA) to assess the specificity and sensitivity for each target with regard to its cellular localization, subcellular localization, and co-expression of proteins across different tissue types (Figures S1A and S1B). When a negative tissue control was unavailable, appropriate fields of view with both antigen-positive and negative internal control cells were evaluated, therefore serving as internal validation. The TMA included spleen, tonsil, lymph node, colon and placenta tissues. Six serial dilutions were performed for each antibody to identify the working titer that yielded maximal separation between signal and noise across tissues. Marker validation was further corroborated on the same TMA by single-plex chromogenic IHC to assure that the test performs as expected.

MIBI-TOF imaging

Imaging was performed using a MIBI-TOF instrument with a Hyperion ion source. Xe+ primary ions were used to sequentially sputter pixels for a given FOV.

In situ hybridization studies

In Situ Hybridization (ISH) studies with the commercially available kit was performed according to the manufacturer's recommendations with minor variations according to the tissue type (ACDBio). Briefly, a viable recut for the detection of mRNA was obtained after shaving a few times the gastric FFPE tissue block. The FFPE tissue section along with tissue controls were baked, deparaffinized and incubated with RNAscope® Hydrogen Peroxide solution (#322335) for 10 min at room temperature. Antigen retrieval was carried out in 1X RNAscope® Target retrieval solution (#322000) for 15 min at 100°C followed by protease digestion for 30 min at 40°C. The experimental approach to validate the mRNA IFN-γ detection in gastric tissue is reported in Figure S2A. Assay control along with IFN-γ controls in serial sections of tissue microarrays were performed in parallel with the gastric biopsy for the detection of IFN-γ transcript by single-plex ISH (Figure S2B). Single-plex ISH detection for human IFN-γ (#310501), Positive Control Probe (human PPIB, #313901) and Negative Control Probe (DapB, #310043) was carried out using RNAscope® 2.5 HD Reagent Kit-Red (#322360) in control slides (HeLa cell pellet, #310045). For the analysis of IFNG transcript in healthy stomach tissues, the RNAscope® 2.5 HD Assay- Brown

(#322310) kit was used with positive control probe UBC (Hs-UBC, #5101512) in place of PPIB, and target retrieval was performed for 30 min. Target probes were hybridized for 2 h at 40°C using HybEZ oven, followed by a series of six amplification steps. Following amplification, slides were stained using a chromogenic substrate (Fast Red or DAB), and finally counterstained using 50% Gill's Hematoxylin (American MasterTech, California) before evaluation by light microscopy. Each single RNA transcript appears as a distinct dot of red chromogen precipitate visible by bright field microscope.

QUANTIFICATION AND STATISTICAL ANALYSIS

Single-cell segmentation

Multiplexed image sets were extracted, slide background subtracted, denoised, and aggregate filtered as previously described.[20] Segmentation was performed using the Mesmer CNN architecture.[30] The nuclear marker HH3 and membrane markers CD45, HLA-DR, HLA-Class I, and NaKATPase were used as input data to the segmentation model. Single cell expression profiles were extracted from the segmentation masks.

Dataset normalization and clustering

Cells were first normalized by cell size and arcsinh-transformed. Cells were then normalized by their total expression, such that the total expression of each cell was equal to 1. A 99.9% normalization was applied for each marker across all cells. Cells were clustered into 100 clusters using FlowSOM.[31] based on the expression of 14 markers: CD45, CD20, CD3, CD4, CD8, CD68, CD14, CD209, CD56, Mast Cell Chymase, CD31, Vimentin, SMA, Pan-Keratin. For the control samples, clustering was based on these 14 markers: CD45, CD20, CD3, CD4, CD8, CD68, CD14, CD209, Mast Cell Chymase, Mast Cell Tryptase, CD31, Vimentin, SMA, Pan-Keratin. The average expression of each of the 100 clusters was found and the z-score for each marker across the 100 clusters was computed. Using the z-scored mean expression values for each marker, the clusters were given a cell annotation. IFN-γ+ cells were annotated as cells with IFN-γ signal greater than the 75th percentile of all non-zero IFN-γ expression. FoxP3+ CD4+ cells and Granzyme B+ CD8+ cells were annotated in a similar manner.

Statistical analyses

Data was first tested for normality with the Shapiro-Wilk test and D'Agostino & Pearson test. Normally distributed data was compared between two groups with the two-tailed Welch's t test. Nonparametric data was compared using the Mann–Whitney U Test. To determine cell density, the total tissue area for each point was calculated. The extracted carbon channel TIF was first Gaussian blurred using a radius of 2, then Otsu's method was used to determine a threshold for binarization. The pixels in this binarized mask were summed together, then converted to mm^2. Cell density was calculated by dividing cell counts by tissue area.

Software

Image processing was conducted with MATLAB 2019a. Statistical analysis was conducted in R v3.6.0 and Python 3.7.9. Data visualization and plots were generated in R v3.6.0 and Prism v9. Representative images were processed in Adobe Photoshop CC2019. Schematic visualizations were produced with Biorender.